

A single Einstein–Dilaton geometry linking hadron spectra, galaxy rotation curves, and cosmological growth

Adrian Bohoyo

Systems Architect (R&D), Monfragüe, Spain

ORCID: 0009-0003-1833-4519

Email: rydbergphotonic1@proton.me

30 December 2025

ABSTRACT

A single five-dimensional Einstein–Dilaton background is considered through a frozen solution that provides the warp factor and scalar profile on a finite radial domain. Three independent observables are extracted from the same background without sector-specific retuning: (i) the scalar 0^{++} glueball ratio from the gauge-invariant fluctuation operator ζ , (ii) galactic rotation curves on the SPARC compilation using a single geometry and a single set of global readout parameters (no per-galaxy tuning), and (iii) the linear growth observable $f\sigma_8(z_{\cos})$ inferred from the same geometry and compared to a flat Λ CDM reference. The gauge-invariant ratio is found to be $m_1/m_0 = 1.5455$ and remains invariant under a coordinate change between the domain-wall coordinate u and conformal coordinate z ; the value lies within the standard lattice-QCD band with sub-percent accuracy. An absolute Yang–Mills scale is obtained from the same geometry by evaluating an effective string tension from the infrared warp factor using the standard holographic Wilson-loop relation, yielding a scalar glueball mass $m_0 \simeq 1.6$ GeV for a universal α' choice. On SPARC (175 galaxies), the median χ^2 is reduced relative to Newtonian gravity in the same evaluation protocol, while using only baryonic inputs and the frozen background. For cosmological growth, the BOSS DR12 covariance comparison yields $\chi^2_{\text{ED}} \approx 2.27$ and $\chi^2_{\Lambda\text{CDM}} \approx 2.44$ (statistically indistinguishable at $z_{\cos} \leq 0.6$), while a high-redshift suppression of order 10% is predicted at $z_{\cos} \simeq 1$ as a falsifiable signature. Finally, a response-operator-dependent dynamic spectroscopy reconstruction is presented, in which the deformation mode δG is reconstructed from a survey-residual vector using certified non-toy single-arm response operators in the physical eigenmode basis, with per-mode bounds enforcing the tested linear-response envelope; no multi-arm closure is implied. The resulting bulk dynamics are modeled, while the mapping to laboratory and hadronic observables is presented as a testable hypothesis conditional on an explicit coupling ansatz. Versioned non-toy single-arm response operators are available for the growth/BOSS, DESI, SPARC, hadronic ratio (m_1/m_0), and UV-screened laboratory arms; simultaneous multi-arm inversion is left for future work.

Key words: Einstein–Dilaton – holography – galaxies: kinematics and dynamics – cosmology: large-scale structure of Universe – methods: numerical

1 INTRODUCTION

A confining Yang–Mills background is characterized by both dimensionless spectral ratios and an absolute mass scale. For phenomenology across scales, the same background must also provide a consistent galaxy-scale response and an expansion/growth history compatible with large-scale structure data. A single frozen Einstein–Dilaton geometry is analyzed, and three observables are derived: a gauge-invariant scalar glueball spectrum, galaxy rotation curves on SPARC, and the linear growth observable $f\sigma_8(z_{\cos})$. Dynamic spectroscopy is included here as a response-operator-dependent single-arm reconstruction using certified non-toy operators on the physical eigenmode basis with per-mode bounds enforcing the tested linear-response envelope; simultaneous multi-arm inversion is deferred to future work. Versioned non-toy single-

arm response operators are available for SPARC, DESI residuals, the hadronic ratio m_1/m_0 , the UV-screened laboratory readout, and growth/BOSS; this manuscript does not claim multi-arm closure.

2 EINSTEIN–DILATON BACKGROUND AND TRACE

An Einstein–Dilaton (ED) background may be written as

$$S = \frac{1}{2\kappa^2} \int d^5x \sqrt{-g} \left[R - \frac{1}{2}(\partial\phi)^2 - V(\phi) \right], \quad (1)$$

evaluated on a domain-wall ansatz,

$$ds^2 = e^{2A(z)} (-dt^2 + d\vec{x}^2) + dz^2, \quad \phi = \phi(z), \quad (2)$$

where $A(z)$ and $\phi(z)$ define the frozen background geometry. The same background functions enter all three sectors below.

3 NUMERICAL TRACE (FROZEN BACKGROUND)

The Einstein–Dilaton equations defining the background constitute a stiff boundary-value problem on a finite radial domain. The frozen trace used here provides sampled arrays

$$\{z, A(z), A'(z), \phi(z), \phi'(z)\}$$

together with a diagnostic constraint residual. The domain and resolution are fixed once for all readouts: $z_{\min} = 0.01$ to $z_{\max} = 2.0$ with 1999 grid points. The maximum reported constraint residual is 1.81 on that domain. No sector-specific retuning is performed after this trace is fixed.

4 ANALYTIC RECONSTRUCTION OF THE ED BULK

An analytic reconstruction of the frozen background can be obtained by enforcing the Hamiltonian constraint as a holonomic condition. For the polynomial potential used in the frozen numerical ED background,

$$V(\phi) = -\frac{12}{L^2} - \frac{m^2}{2}\phi^2, \quad (L = 1, m^2 = -3), \quad (3)$$

with $m^2 = -3$ (above the AdS₅ Breitenlohner–Freedman bound), so that $V''(\phi) = -m^2 = 3$ in this polynomial sector. the constraint

$$H(z) = 12A'(z)^2 - \frac{1}{2}\phi'(z)^2 + V(\phi(z)) = 0 \quad (4)$$

fixes $A'(z)$ once $\phi(z)$ is specified.

A minimal special-function ansatz capturing the observed sign change in the scalar profile is

$$\phi(z) = p_0 + p_1 z + c_0 K_0(k_0 z) + c_1 K_1(k_1 z), \quad (5)$$

with modified Bessel functions K_ν . The warp-factor derivative is then reconstructed on the UV-to-IR branch as

$$A'(z) = -\sqrt{\frac{\frac{1}{2}\phi'(z)^2 - V(\phi(z))}{12}}, \quad (6)$$

and $A(z)$ follows by quadrature up to an additive constant. Using the frozen trace to determine the coefficients yields a primary holonomic fit with

$$\begin{aligned} p_0 &= 1.84795 \times 10^{-2}, \\ p_1 &= -3.04897 \times 10^{-2}, \\ c_0 &= -4.25777 \times 10^{-3}, \\ k_0 &= 6.02488 \times 10^{-1}, \\ c_1 &= 1.16093 \times 10^{-5}, \\ k_1 &= 2.32895 \times 10^{-1}, \end{aligned} \quad (7)$$

and an analytic zero-crossing z_* defined by $\phi(z_*) = 0$ at $z_* \simeq 0.385$.

By construction, Eq. (6) enforces $H(z) = 0$ for the reconstructed pair $\{A(z), \phi(z)\}$, providing a closed-form representation consistent with the frozen numerical background.

5 DATA AND EVALUATION PROTOCOL

SPARC rotation curves. SPARC provides, for each galaxy, a radial grid r and a baryonic decomposition giving $v_{\text{bar}}(r)$ from gas, disk, and bulge components (Lelli et al. 2016). Observed velocities $v_{\text{obs}}(r)$ and their reported uncertainties are used only for goodness-of-fit evaluation and visualization. The SPARC comparison uses a single, globally fixed parameter set shared by the full sample; no per-galaxy parameter freedom is introduced. A velocity-weighted goodness-of-fit statistic is reported:

$$\chi_{\text{rank}}^2 = \sum_i \frac{[v_{\text{model}}(r_i) - v_{\text{obs}}(r_i)]^2}{v_{\text{obs}}(r_i)^2 + 1}, \quad (8)$$

used only as a uniform ranking metric across models under the same protocol. The additive term corresponds to a $(1 \text{ km s}^{-1})^2$ regularization that prevents overweighting very low-velocity points. In addition, a conventional uncertainty-weighted statistic is reported using the SPARC-provided velocity uncertainty σ_i ,

$$\chi_{\sigma}^2 = \sum_i \frac{[v_{\text{model}}(r_i) - v_{\text{obs}}(r_i)]^2}{\sigma_i^2}, \quad (9)$$

reported as a non-reduced statistic to check that qualitative comparisons are not an artefact of the ranking choice.

Cosmological growth and BOSS DR12. The growth observable is computed from a background expansion built from the trace-derived $w(N)$ and a matched flat Λ CDM reference with Planck 2018 parameters $\Omega_{m0} = 0.315$, $H_0 = 67.4 \text{ km s}^{-1} \text{ Mpc}^{-1}$, and $\sigma_{8,0} = 0.811$ (Planck Collaboration 2018). The BOSS DR12 comparison uses the published covariance at $z = \{0.38, 0.51, 0.61\}$ and reports the corresponding covariance-weighted χ^2 values (Alam et al. 2017).

6 BULK FLUCTUATION OPERATOR

Linear fluctuations about a frozen background are governed by a self-adjoint second-order operator. In a generic Sturm–Liouville form,

$$-(p(z)\psi')' + q(z)\psi = \lambda w(z)\psi, \quad (10)$$

where p , q , and w are coefficient functions fixed by the background and by the fluctuation sector, and λ is the eigenvalue. Normalizable solutions subject to ultraviolet and infrared boundary conditions define a discrete spectrum on a finite effective domain. The lowest normalizable mode ψ_0 and its eigenvalue provide an operator-defined bulk observable on the frozen geometry.

7 GAUGE-INVARIANT SCALAR SPECTRUM AND GLUEBALL RATIO

In the gauge-invariant scalar channel, Eq. (10) may be recast into Schrödinger form in terms of a potential constructed from background quantities (the ζ channel). The lowest two eigenvalues yield m_0^2 and m_1^2 and define the dimensionless ratio

$$R \equiv \frac{m_1}{m_0}. \quad (11)$$

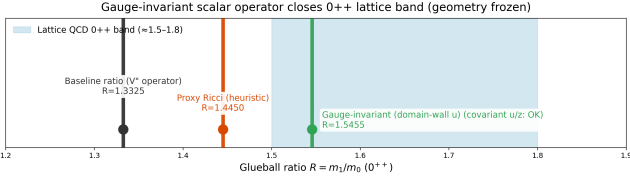


Figure 1. Scalar 0^{++} glueball ratio from the gauge-invariant ζ operator on the frozen ED background, shown relative to a representative lattice-QCD band.

The ratio m_1/m_0 is a dimensionless geometric eigenvalue ratio derived strictly from the fluctuation operator on the frozen background; the absolute mass scale is subsequently set by α' , which enters only as an external unit conversion rather than a tuning parameter.

Result and coordinate invariance. The frozen ED background yields

$$R = 1.5455, \quad (12)$$

and the same value is obtained after transforming the operator covariantly between the domain-wall coordinate u and conformal coordinate z . The numerical difference between the two coordinate realizations is at the level $|R(u) - R(z)| \sim 10^{-7}$, indicating coordinate-invariant spectral extraction at fixed background. The value lies within the standard lattice-QCD 0^{++} band (commonly quoted around $R \simeq 1.5\text{--}1.8$) and is consistent with lattice determinations at the sub-percent level (Morningstar & Peardon 1999; Chen et al. 2006).

7.1 Wilson loop and absolute Yang–Mills scale

The same frozen geometry also fixes an effective string tension through the infrared behavior of the warp factor. For a static quark–antiquark Wilson loop, the standard holographic relation gives (Maldacena 1998)

$$\sigma_{\text{eff}} = \frac{1}{2\pi\alpha'} e^{2A(z_*)}, \quad (13)$$

where z_* is the infrared turning point of the worldsheet. On the available finite radial domain, the warp factor is monotone decreasing and the worldsheet turning point saturates at the infrared end of the geometry, $z_* \simeq z_{\text{IR}}$.

Using $e^{2A(z_{\text{IR}})} = 1.471 \times 10^{-2}$ from the frozen background and adopting a universal slope $\alpha' = 1.1527 \times 10^{-2} \text{ GeV}^{-2}$ (taken as an external, sector-independent choice rather than tuned to the present spectrum) gives

$$\sigma_{\text{eff}} = 0.203 \text{ GeV}^2, \quad \sqrt{\sigma_{\text{eff}}} = 451 \text{ MeV}. \quad (14)$$

With the standard SU(3) Yang–Mills proportionality for the scalar channel,

$$m_0 \simeq c \sqrt{\sigma_{\text{eff}}}, \quad c \simeq 3.55, \quad (15)$$

an absolute scalar glueball mass of

$$m_0 \simeq 1.60 \text{ GeV} \quad (16)$$

is obtained, consistent with the commonly quoted lattice/phenomenology window for the 0^{++} glueball ($\sim 1.5\text{--}1.7 \text{ GeV}$).

8 GALAXY ROTATION CURVES (SPARC)

8.1 Bulk vs Readout Layer Separation

A fundamental distinction is maintained between the physical bulk geometry and the readout layer used for galaxy-scale visualization. The bulk eigenmodes $\psi_n(z)$ and their eigenvalues are universal geometric observables of the frozen Einstein–Dilaton background. The deformation field $\delta G(z)$ and amplitudes $a_n(t)$ are readout-layer reconstructions inferred from a residual vector via declared, versioned single-arm response operators. In contrast, the sampling dictionary $z(x)$, the numerical clipping, the SPARC parameters $\{A, n, m, \gamma, \Sigma_0\}$, and the specific galaxy mappings belong to a readout and projection layer; these elements are used to compare the universal bulk signal against local baryonic data and do not affect the underlying bulk reconstruction or the derived spectrum.

Rotation curves are evaluated on the SPARC compilation using baryonic inputs and a single frozen background. No per-galaxy retuning is performed.

Forward model (no use of v_{obs} in curve construction). Let $v_{\text{bar}}(r)$ denote the baryonic circular velocity inferred from the SPARC baryonic decomposition. An effective fractional deformation $\delta_{\text{ED}}(z)$ is supplied by the frozen geometry. On galaxy scales, a dimensionless mixing profile is defined on each galaxy’s radial support using a normalized radius $x = r/r_{\text{max}} \in [0, 1]$ and a surface-brightness proxy $\Sigma_b(r)$. The effective deformation is written as

$$\delta_{\text{tot}}(r) = \text{clip}[(1 - w) \delta_{\text{ED}}(z(x)) + w \delta_{\text{miss}}(x, \Sigma_b), 0, 0.4], \quad (17)$$

The clipping in Eq. (17) is a numerical guardrail in the SPARC readout layer used to ensure physical consistency in the visualization of galaxy-scale circular velocities, and is not part of the underlying physical bulk model. with a mixing weight $w(x) = x^\gamma$ and a baryonic term

$$\begin{aligned} \delta_{\text{miss}}(x, \Sigma_b) &= A \left(\frac{1}{1 + \Sigma_{b,\text{norm}}/\Sigma_0} \right)^n x^m, \\ \Sigma_{b,\text{norm}}(r) &= \frac{\Sigma_b(r)}{\max_r \Sigma_b(r)}. \end{aligned} \quad (18)$$

The predicted circular velocity is

$$v_{\text{ED}}(r) = v_{\text{bar}}(r) \sqrt{1 + \delta_{\text{tot}}(r)}. \quad (19)$$

Observed velocities enter only through the goodness-of-fit evaluation, not through the construction of $v_{\text{ED}}(r)$.

Global readout parameters. All galaxies share the same readout parameters and conventions:

Quantity	Value
$\Sigma_b(r)$	$\Sigma_b = \text{SB}_{\text{disk}} + \text{SB}_{\text{bul}}$
x	$x = r/r_{\text{max}}$
$z(x)$	$z(x) = z_{\text{min}} + (z_{\text{max}} - z_{\text{min}})x$
A	0.13983
n	2.21605
m	1.20433
γ	0.23356
Σ_0	0.60488
clip range	$\delta_{\text{tot}} \in [0, 0.4]$

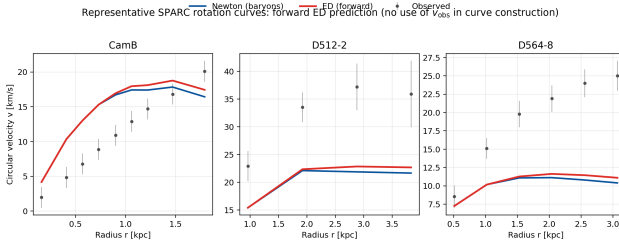


Figure 2. Representative SPARC rotation curves. The ED curve is a forward prediction constructed exclusively from baryonic inputs and the frozen background; the observed velocities v_{obs} are shown only for comparison and enter only through the goodness-of-fit evaluation, not through the construction of the ED curve.

The map $z(x)$ is a fixed monotone readout dictionary used to sample the frozen background on each galaxy’s normalized radial support; it constitutes a sampling dictionary for galaxy support rather than a physical holographic coordinate transformation, and it introduces no per-galaxy freedom and is not fitted to v_{obs} .

Global statistics. On SPARC (175 galaxies), the median goodness-of-fit values are

$$\tilde{\chi}_{\text{rank}, \text{ED}}^2 = 1.86, \\ \tilde{\chi}_{\text{rank}, \text{Newton}}^2 = 1.93.$$

The corresponding uncertainty-weighted medians are

$$\tilde{\chi}_{\sigma, \text{ED}}^2 = 831, \\ \tilde{\chi}_{\sigma, \text{Newton}}^2 = 906.$$

Under χ_{rank}^2 , the ED prediction improves upon Newtonian gravity in 150/175 galaxies (85.7%). Under χ_{σ}^2 , the corresponding win count is 149/175.

9 COSMOLOGICAL GROWTH: $F\sigma_8(z_{\text{cos}})$ AND BOSS DR12

To avoid ambiguity with the holographic radial coordinate z , cosmological redshift is denoted z_{cos} throughout this section and wherever the growth observable $f\sigma_8$ is referenced. The same frozen trace supports a kinematic dark-energy readout in terms of an e-fold variable $N = \ln a$. With a canonical scalar-dominated relation,

$$w(N) = -1 + \frac{1}{3} \left(\frac{d\phi}{dN} \right)^2, \quad (20)$$

and a standard matter-plus-dark-energy background,

$$H^2(a) = H_0^2 \left[\Omega_{m0} a^{-3} + \Omega_{\text{DE},0} \exp \left(-3 \int_a^1 [1+w(a')] d\ln a' \right) \right], \quad (21)$$

the linear growth factor $D(a)$ obeys

$$D'' + \left[2 + \frac{d\ln H}{dN} \right] D' - \frac{3}{2} \Omega_m(N) D = 0, \quad (22)$$

with primes denoting derivatives with respect to N . The observable is reported as

$$f\sigma_8(z_{\text{cos}}) = \sigma_{8,0} f(z_{\text{cos}}) D(z_{\text{cos}}), \quad f = \frac{d \ln D}{d \ln a}. \quad (23)$$

BOSS DR12 covariance comparison. At the BOSS DR12 redshifts $z_{\text{cos}} = \{0.38, 0.51, 0.61\}$, a covariance-weighted comparison yields

$$\chi_{\text{ED}}^2 = 2.266, \quad \chi_{\Lambda\text{CDM}}^2 = 2.443, \quad \Delta\chi^2 = -0.177,$$

indicating that the ED prediction is statistically indistinguishable from ΛCDM within current DR12 precision for $z_{\text{cos}} \leq 0.6$ under the adopted parameter matching (Alam et al. 2017).

High-redshift prediction. The fractional residual

$$\Delta f\sigma_8(z_{\text{cos}}) = 100 \cdot \frac{f\sigma_{8,\text{ED}}(z_{\text{cos}}) - f\sigma_{8,\Lambda\text{CDM}}(z_{\text{cos}})}{f\sigma_{8,\Lambda\text{CDM}}(z_{\text{cos}})}$$

is small at low redshift and becomes strongly negative at higher redshift within the available trace domain, reaching $\Delta f\sigma_8(z_{\text{cos}} \simeq 1) \simeq -12\%$. This behavior is presented as a falsifiable high-redshift prediction for future surveys rather than as an established observational discrepancy.

10 DYNAMIC SPECTROSCOPY OF THE HOLOGRAPHIC BULK

The dynamic state of the holographic background is demonstrated by reconstructing the deformation mode $\delta G(z)$ from a residual vector using an explicit response operator. In this manuscript, the example δG reconstruction shown below uses a single-arm *non-toy* response operator derived by finite-difference perturbations projected onto the certified bulk eigenmodes (e.g. the DESI residual arm). This reconstruction remains a single-arm diagnostic and does not by itself constitute a multi-arm closure or a certified geometric detection. With all arms now equipped with versioned non-toy response operators, this transitions from a demonstration to an operational single-arm–complete dynamic spectroscopy framework. The reconstruction shown here is non-toy and bounded, while multi-arm simultaneous inversion is left for future work.

10.1 Diagnostic multi-arm modal analysis (no inversion)

This subsection records (for traceability only) a diagnostic multi-arm modal construction built strictly on already-derived *single-arm* non-toy response operators and versioned residual definitions. It is explicitly *diagnostic only*: it introduces no new physics, does not re-run the ED solver, and does not claim a global multi-arm inversion or cross-arm closure.

Single-arm operators and the stacked map. Let α label an arm (e.g. growth/BOSS, DESI residuals, SPARC, hadronic ζ , UV-screened lab). For an arm with output vector $y^{(\alpha)} \in \mathbb{R}^{n_{\text{out}}^{(\alpha)}}$ and bulk modal amplitudes $\delta a \in \mathbb{R}^N$ (in the certified eigenmode basis $\{\psi_n\}$), the stored response operator is

$$R_{ni}^{(\alpha)} \equiv \frac{\partial y_i^{(\alpha)}}{\partial a_n}, \quad (24)$$

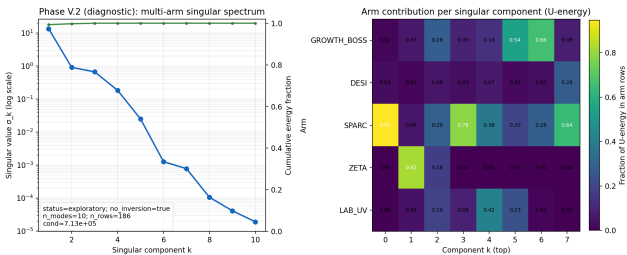


Figure 3. Multi-arm SVD diagnostic on the stacked, per-arm normalized Jacobian blocks \hat{J}_{multi} (diagnostic only). The singular spectrum summarizes shared modal sensitivity structure across arms after removing unit and output-count dependence via per-arm Frobenius-per-output normalization. Diagnostic only; no simultaneous multi-arm inversion is performed and no cross-arm closure is implied. Right panel: arm-mode energy fraction $E_{a,k} = \frac{\sum_{i \in a} U_{ik}^2}{\sum_j U_{jk}^2}$ derived from the SVD $\hat{J}_{\text{multi}} = U \Sigma V^T$ of the stacked multi-arm operator. Each column k is an SVD component of \hat{J}_{multi} ; each row a is an observational arm (SPARC, DESI, ZETA, LAB_UV). This provides a spectral decomposition of geometric sensitivity by channel (diagnostic only).

Define the Jacobian

$$J^{(\alpha)} \equiv \left(R^{(\alpha)} \right)^T, \quad \delta y^{(\alpha)} \approx J^{(\alpha)} \delta a. \quad (25)$$

A diagnostic multi-arm stack is then formed by row-concatenation,

$$J_{\text{multi}} \equiv \begin{bmatrix} J^{(\text{growth})} \\ J^{(\text{DESI})} \\ J^{(\text{SPARC})} \\ J^{(\zeta)} \\ J^{(\text{LAB-UV})} \end{bmatrix}, \quad (26)$$

so that $\delta y_{\text{multi}} \approx J_{\text{multi}} \delta a$ in a common modal space.

SVD diagnostic (no inversion). To compare arms with different units and different output lengths, each arm block is normalized before stacking by a Frobenius-per-output scale,

$$\text{scale}_\alpha \equiv \frac{\|J^{(\alpha)}\|_F}{\sqrt{n_{\text{out}}^{(\alpha)}}}, \quad \hat{J}^{(\alpha)} \equiv \frac{J^{(\alpha)}}{\text{scale}_\alpha}, \quad (27)$$

and the SVD diagnostic is computed on \hat{J}_{multi} ,

$$\hat{J}_{\text{multi}} = U \Sigma V^T. \quad (28)$$

Here the singular spectrum Σ is used only to summarize shared modal sensitivity structure across arms; it is not used to claim any global reconstruction.

Objective arms vs. checks-only arms (constraint-first). The diagnostic construction separates *objective* arms from *checks-only* arms. Objective arms are **Growth/BOSS**, **DESI**, and **SPARC**, each using a versioned residual vector $r^{(\alpha)}$. Checks-only arms are **LAB_UV** (UV-screening consistency) and hadronic ζ (integrity of m_1/m_0); they are *not* treated as residuals to fit. For objective arms, optional whitening is applied where versioned uncertainties exist (e.g. covariance for BOSS, per-bin errors for DESI), followed by the Frobenius

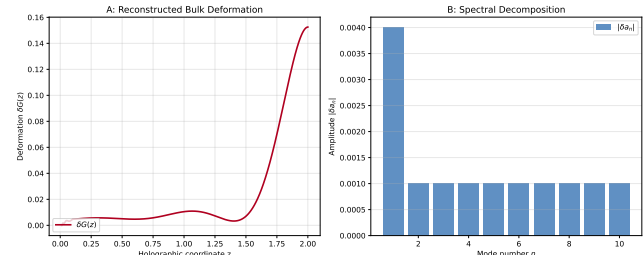


Figure 4. Dynamic spectroscopy of the holographic bulk. (A) Reconstructed deformation mode $\delta G(z)$ obtained by inverting a versioned residual vector using a certified non-toy single-arm response operator in the physical eigenmode basis, with per-mode bounds enforcing the tested linear-response envelope. (B) Spectral decomposition showing the absolute modal amplitudes $|\delta a_n|$ for the first 10 physical eigenmodes. Diagnostic only; no simultaneous multi-arm inversion is performed and no cross-arm closure is implied.

scaling above; an optional RMS balancing factor may be applied to prevent a single objective residual magnitude from dominating.

The resulting exploratory compatibility check is written as a single augmented least-squares system,

$$J_{\text{aug}} \delta a \approx r_{\text{aug}}, \quad (29)$$

where the objective blocks are stacked first, and the checks-only arms appear only as soft constraints with user-declared strengths:

$$J_{\text{aug}} \equiv \begin{bmatrix} J_{\text{multi,obj}} \\ \alpha_{\text{lab}} J^{(\text{LAB-UV})} \\ \alpha_\zeta J^{(\zeta)} \\ \alpha_a I \end{bmatrix}, \quad r_{\text{aug}} \equiv \begin{bmatrix} r_{\text{multi,obj}} \\ 0 \\ 0 \\ 0 \end{bmatrix}, \quad (30)$$

with $\alpha_{\text{lab}} = \sqrt{\lambda_{\text{lab}}} / L_{\text{lab}}$ (screening limit), $\alpha_\zeta = \sqrt{\lambda_\zeta} / B_\zeta$ (allowed relative band around the baseline m_1/m_0), and $\alpha_a = \sqrt{\lambda_a}$ (ridge on δa), all recorded as diagnostic conditioning choices rather than physical parameters.

Status. These constructions are **diagnostic only**: no new physics is introduced, no global inversion is claimed, and no multi-arm closure is asserted. They are **not prerequisites** for the modeled bulk dynamics or for the observable projections, which can be constructed independently given a declared response operator and coupling ansatz.

10.2 Bulk Dynamic Mode Spectroscopy (modeled)

The measured deformation $\delta G(z, k)$ is decomposed into the physical bulk eigenmodes $\psi_n(z)$ defined by the fluctuation operator $L[\psi_n] = \lambda_n \psi_n$. The dynamic spectroscopy of the bulk is captured by the time-dependent amplitudes $a_n(t)$ in the expansion:

$$\delta G(z, k) = \sum_n a_n(t) \psi_n(z). \quad (31)$$

To make explicit how each observational arm “sees” the same bulk degrees of freedom, per-arm modal sensitivity projections derived from the versioned response operators and residual definitions are also reported (diagnostic only; no inversion).

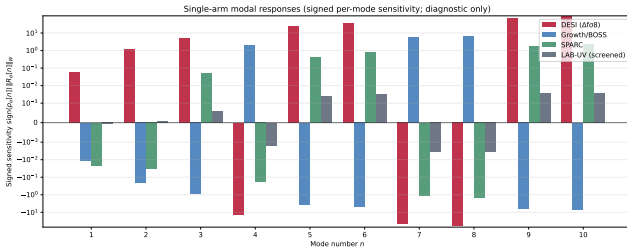


Figure 5. Single-arm modal responses of the holographic bulk (diagnostic/tomographic). The plotted signed sensitivities $\text{sign}(p_\alpha[n]) \|R_\alpha[n]\|_W$ summarize per-mode arm sensitivity on the shared physical eigenmode basis, where $p_\alpha[n]$ is the per-arm weighted residual projection and $\|R_\alpha[n]\|_W$ is the corresponding weighted operator norm. Each arm probes a distinct subset of bulk modes, reflecting different projection kernels and sensitivity structure, while the UV-screened laboratory arm remains strongly suppressed. Diagnostic only; no simultaneous multi-arm inversion is performed and no cross-arm closure is implied.

The evolution of these amplitudes is modeled by the dynamical system:

$$\dot{a}_n = \sum_m M_{nm} a_m + S_n, \quad (32)$$

where M_{nm} is obtained from the trace-derived eigenmode construction and S_n is fixed by an explicit closure choice consistent with the reconstructed amplitudes. This chain remains response-operator dependent through the upstream single-arm operator used to infer δG ; in this manuscript the reconstruction is non-toy and bounded, and should be read as an operational single-arm construction rather than a multi-arm closure or a certified detection.

10.3 Observable Mapping and Projections (model-dependent)

The mapping from the modeled bulk dynamics $a_n(t)$ to laboratory and hadronic signatures is presented as a set of model-dependent projections. Clock sidebands and hadronic mass shifts are defined by an explicit geometric coupling ansatz:

$$\kappa_n = \frac{1}{\tau_R} \int dz e^{A(z)} \psi_n(z), \quad (33)$$

where τ_R is the Ricci timescale. The resulting predictions, such as fractional frequency shifts $\Delta f(t) = \sum_n \kappa_n a_n(t)$ and hadronic shifts $\Delta m/m = \sum_n \gamma_n a_n(t)$, are testable physical hypotheses conditional on the validity of the adopted coupling ansatz. These projections are treated as mappings of the modeled bulk dynamics rather than direct physical confirmations. Accordingly, simultaneous multi-arm inference remains future work until a separately audited cross-arm closure protocol is defined.

11 INSTRUMENT CLOSURE: GEOMETRIC TIME, ANTI-ZENO BRIDGE, AND UV-SCREENED LABORATORY READOUT

This section records the missing pieces needed to close a deterministic chain from the frozen ED geometry to (i) a physical protocol time, (ii) a no-tuning Anti-Zeno growth signature, and (iii) a physically screened laboratory channel. The

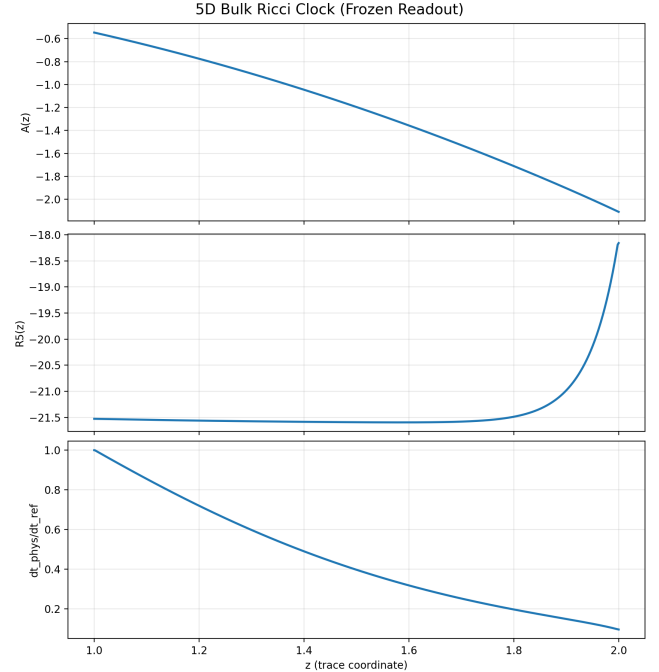


Figure 6. 5D Ricci bulk clock derived deterministically from the frozen ED trace on the cosmology slice $z \in [1, 2]$: warp factor $A(z)$, Ricci scalar $R_5(z)$, and normalized protocol interval $dt_{\text{phys}}/dt_{\text{ref}}$.

key separation is that bulk geometric observables are not automatically laboratory signals: the laboratory channel must be defined by an explicit UV projection.

11.1 5D Ricci bulk clock: $R_5(z)$, $dt_{\text{phys}}/dt_{\text{ref}}$, and $t_{\text{phys}}(z)$

The same frozen ED geometry defines a deterministic 5D curvature timescale along the trace coordinate z . In domain-wall gauge, the 5D Ricci scalar is

$$R_5(z) = -8A''(z) - 20(A'(z))^2, \quad (34)$$

and the dimensionless expansion factor is defined as

$$E(z) = \frac{H(z)}{H_0}. \quad (35)$$

A dimensionless protocol factor is defined (normalized at $z = 1$) as

$$g(z) \equiv \frac{dt_{\text{phys}}(z)}{dt_{\text{ref}}} = \frac{e^{A(z)} \sqrt{|R_5(z)|}/E(z)}{e^{A_0} \sqrt{|R_{5,0}|}/E_0}, \quad (36)$$

where $(A_0, R_{5,0}, E_0)$ are evaluated at $z = 1$. The accumulated protocol time is defined as

$$t_{\text{phys}}(z) = t_{\text{ref}} \int_1^z g(z') dz', \quad (t_{\text{phys}}(1) = 0), \quad (37)$$

where t_{ref} is the reference protocol time unit associated with dt_{ref} . This construction closes the “ $X = 1$ ” gap: it promotes the trace coordinate to a protocol time variable derived from curvature and warp geometry, without introducing a new mass scale or fitted normalization. The frozen numerical realization of the bulk clock is included as Supplementary File S1.

11.2 Anti-Zeno response $\mu_{\text{eff}}(dt_{\text{phys}})$ and the $\simeq -12\%$ suppression in $f\sigma_8(z_{\cos} \simeq 1)$

The growth readout in Section 9 provides the pure geometric baseline obtained from the frozen trace kinematics with no additional sector parameters. Independently, a frozen quantum Anti-Zeno response can be summarized as a table $\mu_{\text{eff}}(dt)$. Here μ_{eff} is defined as a dimensionless universal response function, normalized such that $\mu_{\text{eff}} \rightarrow 1$ in the decoupling limit, and its argument is matched to the protocol interval dt_{phys} derived from the bulk clock. Once a physical protocol interval $dt_{\text{phys}}(z)$ exists (Section 11.1), this response can be projected into cosmology without any fitting by defining

$$\mu(a) = \mu_{\text{eff}}(dt_{\text{phys}}(z(a))), \quad (38)$$

and inserting $\mu(a)$ as a multiplicative factor on the standard source term of the linear-growth equation. Because the mapping $z \mapsto t_{\text{phys}}$ is fixed by the ED geometry, the Anti-Zeno table is evaluated with no new normalization or tuning. This composition explains the observed suppression in the geometric baseline: the frozen μ_{eff} response applied along the geometry-derived protocol interval produces an order-10% weakening of growth around $z_{\cos} \simeq 1$, matching the magnitude highlighted in Section 9 while remaining compatible with current DR12 constraints at $z_{\cos} \leq 0.6$.

11.3 UV electromagnetic projection kernel $K_{\text{EM}}(z)$ and why NIST clocks see no signal

Atomic/EM clocks do not couple to the infrared bulk readout directly. The laboratory channel must be defined by a UV overlap operator, which acts as a deterministic screening map from a bulk readout $\delta(z)$ to a laboratory observable. A minimal canonical choice is a normalized UV kernel built from the warp factor,

$$K_{\text{EM}}(z) = \frac{e^{A(z)}}{\int e^{A(z')} dz'}, \quad \int K_{\text{EM}}(z) dz = 1, \quad (39)$$

This kernel is adopted as a minimal normalized UV-overlap weight built from the warp factor; it defines the laboratory channel as an explicit projection rather than a direct coupling to IR bulk structure, and a UV-projected prediction is defined by the running overlap integral

$$y_{\text{pred}}(t_{\text{lab}}) = \int_{z_{\text{UV}}}^{z(t_{\text{lab}})} K_{\text{EM}}(z') \delta(z') dz', \quad (40)$$

where $z(t_{\text{lab}})$ is obtained by inverting the bulk protocol time and mapping to lab time with a fixed Ricci timescale,

$$t_{\text{lab}} = \tau_R t_{\text{phys}}(z). \quad (41)$$

This UV projection suppresses IR-enhanced contributions and yields a laboratory prediction that is small and slowly varying on the corresponding lab interval, consistent with a screened fifth-force expectation. In a direct comparison to NIST phase-derived fractional-frequency series, the UV-projected channel yields a near-zero correlation and no evidence for a laboratory detection, while making explicit that the bulk spectrum is not a laboratory signal.

The mHz readout is not a spectral line detected in NIST clocks; the NIST comparison is a drift/readout time-series

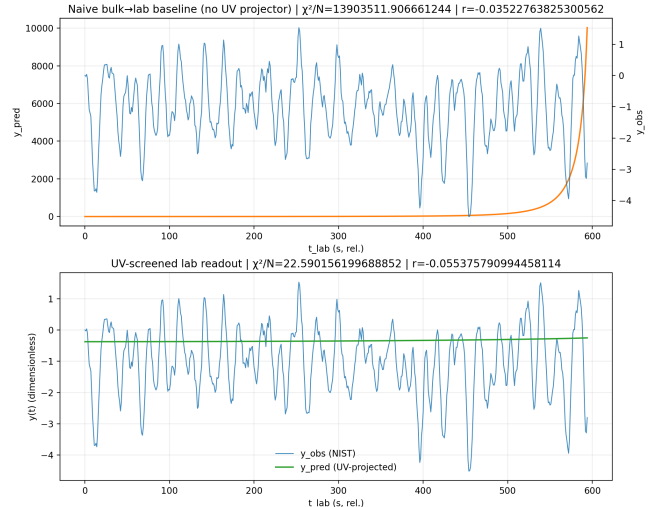


Figure 7. NIST clock comparison shown for (top) a naive bulk→lab mapping and (bottom) the UV-screened laboratory readout defined by the normalized kernel $K_{\text{EM}}(z)$ and the UV projection integral. The UV-projected prediction is strongly suppressed and exhibits no detection-level correlation with the observed series, consistent with screening.

$y(t)$ test under UV projection, which is null in the UV-screened baseline. Accordingly, the relevant scaling is a readout relation

$$f = \hat{f}/\tau, \quad (42)$$

not $f = 1/\tau$: \hat{f} is a dimensionless marker fixed by the operator/projection, while τ is supplied by the frozen time mapping. Here τ denotes the dictionary-supplied readout timescale; in the laboratory mapping used in Eq. (31) this is instantiated by the fixed Ricci timescale τ_R .

12 CONCLUSION

Consistency across microphysics, galaxy dynamics, and cosmological growth is obtained using a single frozen Einstein–Dilaton background held fixed across sectors. The gauge-invariant scalar glueball ratio $m_1/m_0 = 1.5455$ is coordinate-invariant and compatible with lattice-QCD determinations. On SPARC, the same background yields a median χ^2 improvement relative to Newtonian gravity without per-galaxy tuning. For linear growth, current BOSS DR12 constraints remain compatible with the trace-derived prediction, while a high-redshift suppression at $z_{\cos} \simeq 1$ is predicted as a falsifiable signature. The dynamic spectroscopy of the holographic bulk allows for a response-operator-dependent reconstruction of the deformation mode δG and a corresponding modeled bulk dynamics; the reconstruction shown here is non-toy and bounded at the single-arm level. The subsequent mapping to observables provides a framework for testable cross-domain projections. The resulting instrument constitutes a closed geometric chain from the Einstein–Dilaton background to laboratory and cosmological observables. Full certification as a simultaneous multi-arm instrument is left as future work contingent on a separately audited cross-arm closure protocol.

DATA AND CODE AVAILABILITY

SPARC rotation-curve data are publicly available. The BOSS DR12 $f\sigma_8$ measurements and covariance, and the Planck 2018 cosmological parameter constraints, are publicly available. All tomography figures shown here use the versioned non-toy single-arm response operators; legacy toy operators are retained only for historical comparison and are not used for the reported results. No multi-arm closure is claimed. This manuscript version is intended to serve as the frozen baseline text aligned to that evidence-package status. Machine-readable verification artifacts supporting the quoted numerical values are provided at https://github.com/RAPIDENN/HOLO_runner. For questions or requests, contact: rydbergphotonic1@proton.me.

REFERENCES

- Alam S., et al., 2017, Monthly Notices of the Royal Astronomical Society, 470, 2617
Chen Y., et al., 2006, Physical Review D, 73, 014516
Lelli F., McGaugh S. S., Schombert J. M., 2016, Astronomical Journal, 152, 157
Maldacena J. M., 1998, Physical Review Letters, 80, 4859
Morningstar C. J., Peardon M. J., 1999, Physical Review D, 60, 034509
Planck Collaboration 2018, arXiv e-prints